ADVANCED FUNCTIONAL MATERIALS

# Supporting Information

for *Adv. Funct. Mater.*, DOI: 10.1002/adfm.202002868

# Multifunctional Artificial Artery from Direct 3D Printing with Built-In Ferroelectricity and Tissue-Matching Modulus for Real-Time Sensing and Occlusion Monitoring

*Jun Li, Yin Long, Fan Yang, Hao Wei, Ziyi Zhang, Yizhan Wang, Jingyu Wang, Cheng Li, Corey Carlos, Yutao Dong, Yongjun Wu, Weibo Cai, and Xudong Wang**

# Supporting Information

## Multifunctional Artificial Artery from Direct 3D Printing with Built-in Ferroelectricity and Tissue-Matching Modulus for Real-Time Sensing and Occlusion Monitoring

*Jun Li*[1], *Yin Long*[1], *Fan Yang*[1], *Hao Wei*[2], *Ziyi Zhang*[1], *Yizhan Wang*[1], *Jingyu Wang*[1], *Cheng Li*[3], *Corey Carlos*[1], *Yutao Dong*[1], *Yongjun Wu*[3], *Weibo Cai*[2], *Xudong Wang*[1, *]

[1] Department of Materials Science and Engineering, University of Wisconsin-Madison, WI, 53706, USA
[2] Department of Radiology and Medical Physics, University of Wisconsin - Madison, WI, 53705, USA
[3] Laboratory of Dielectric Materials, School of Materials Science and Engineering, Zhejiang University, Hangzhou, 310027, China
E-mail: xudong.wang@wisc.edu

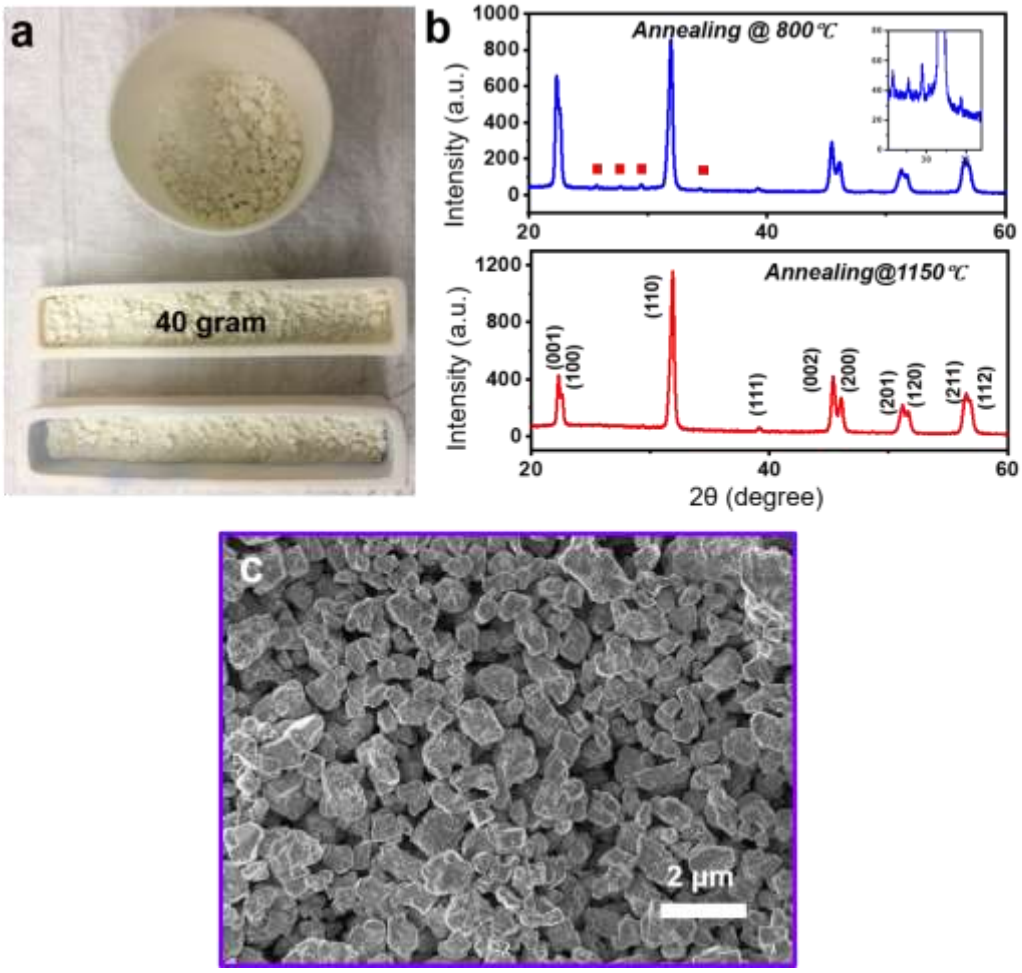


**Figure S1. (a)** 40 gram KNN particles prepared through solid state reaction. **(b)** XRD patterns of KNN particles annealed at 800 ℃ (upper panel) and 1100 ℃ (lower panel). **(c)** SEM image of as-prepared KNN particles.

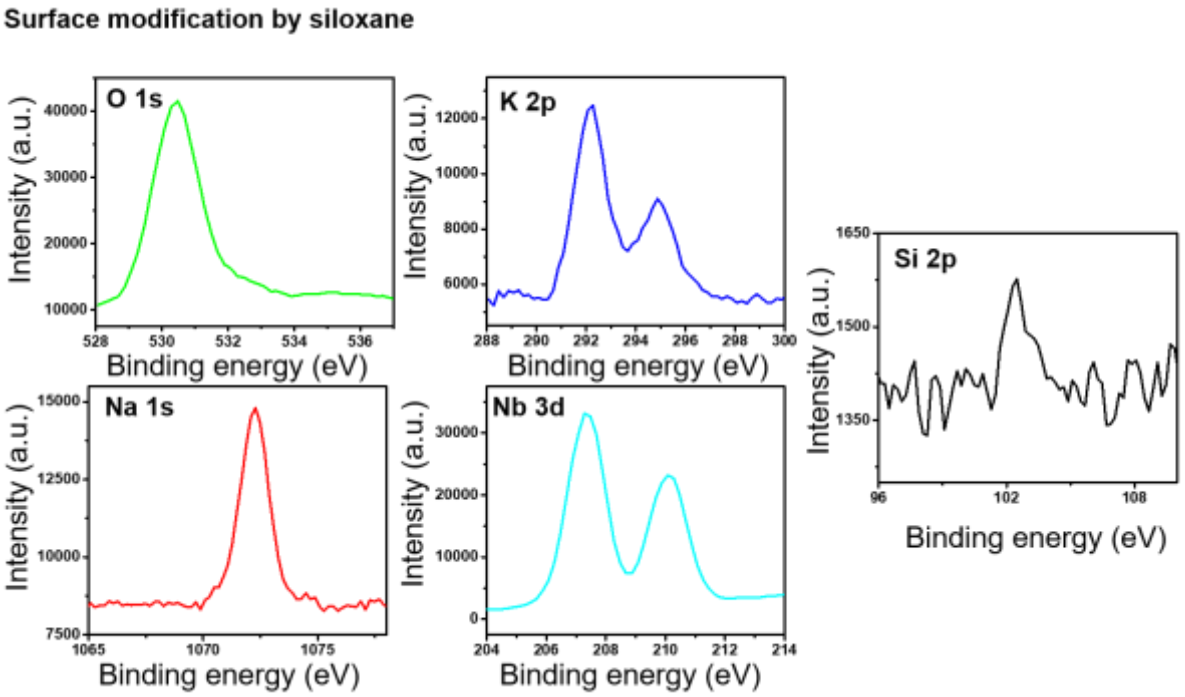


**Figure S2.** XPS spectrum of KNN particles surface functionalized with siloxane.

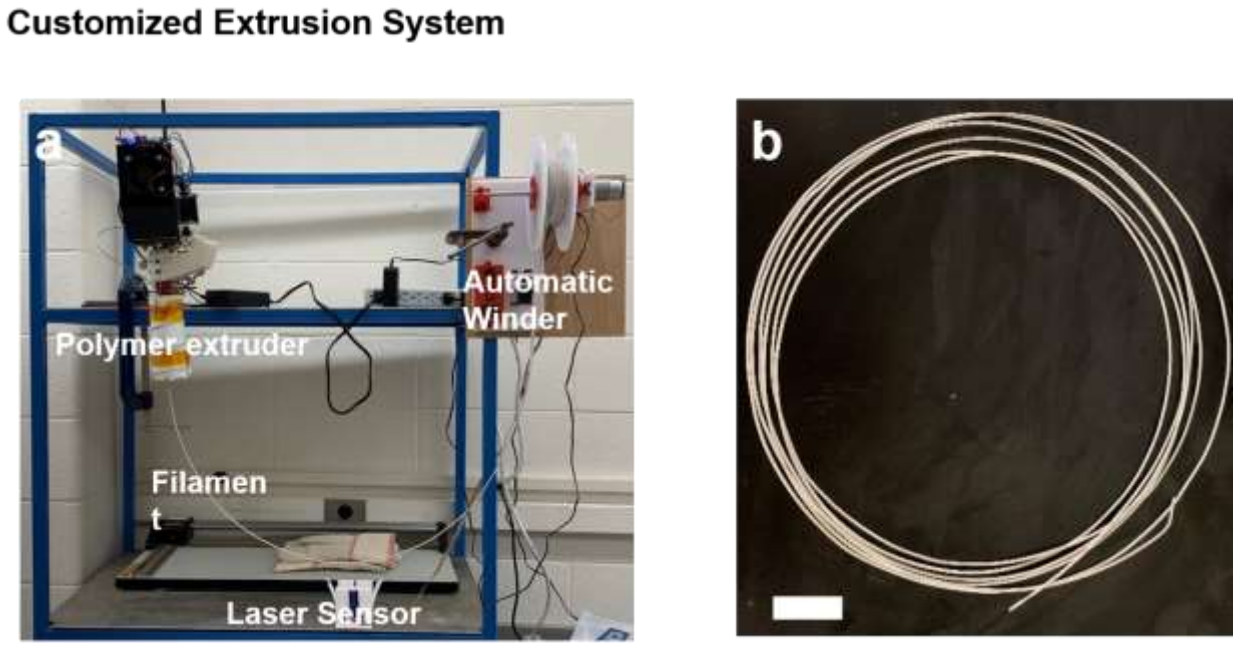


**Figure S3. (a)** Customized polymer extrusion system. **(b)** Digital image of extruded PVDF-KNN filament. The scale bar is 5 cm.

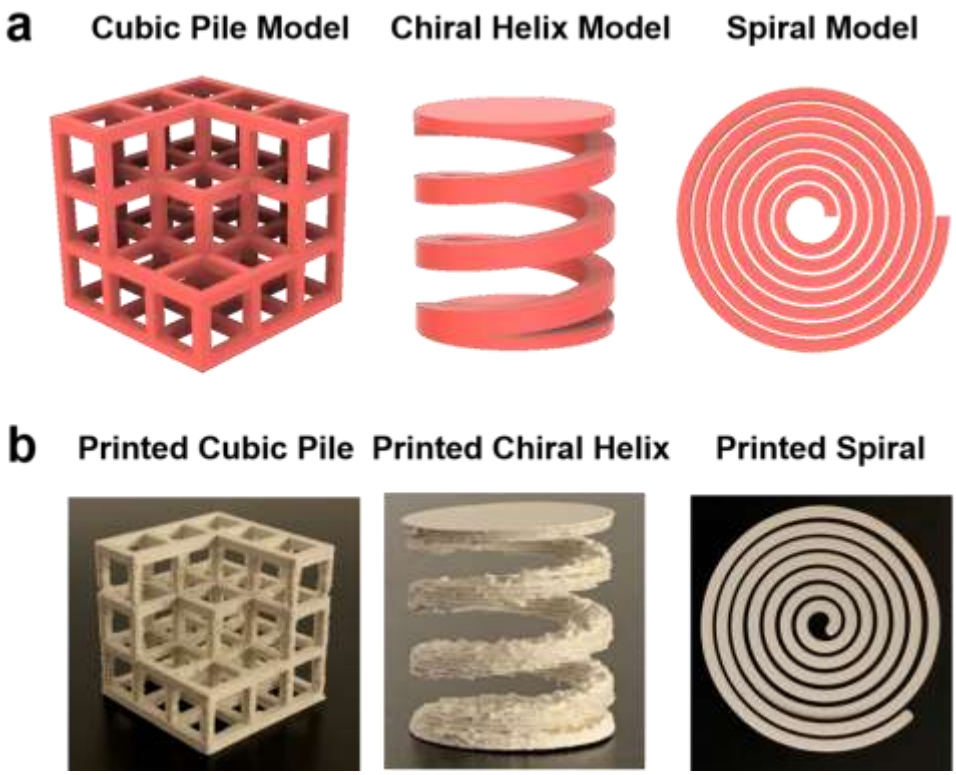


**Figure S4. (a)** Designed models (cubic pile, chiral helix, spiral) for 3d printing. **(b)** Printed objects with good fidelity using PVDF-KNN filament.

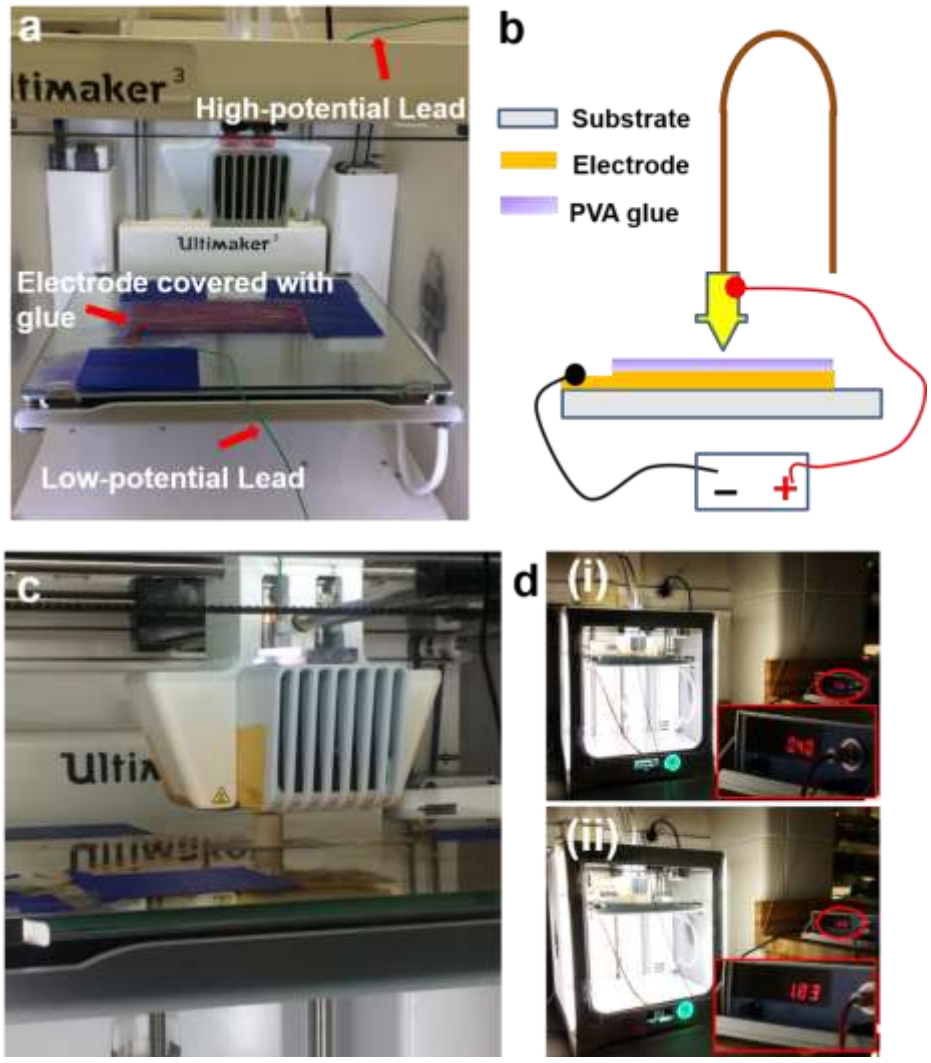


**Figure S5. (a)** Digital image of electric field-assisted printing set-up. **(b)** Schematic illustration of the electric field-assisted FDM technology. **(c)** Real-time piezoelectric cylinder printing. **(d)** Real-time printing under voltage of (i) 400 V and (ii) 1.83 kV.

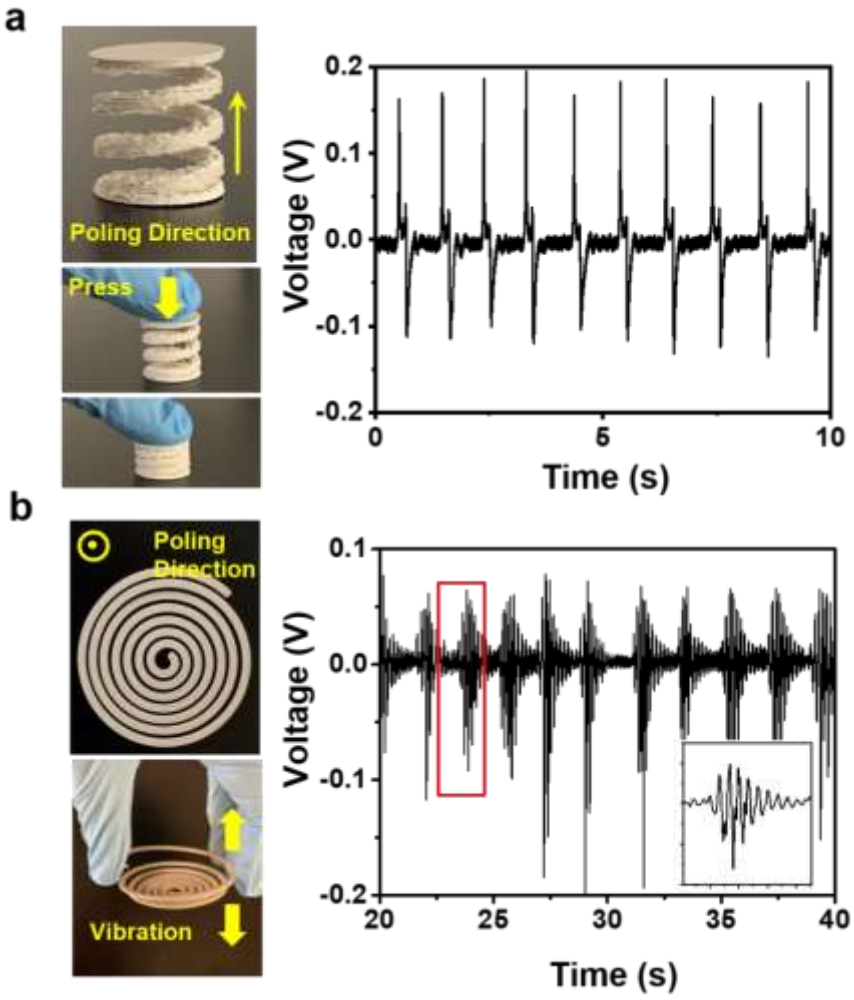


**Figure S6. (a)** As-printed polarized chiral helix and corresponding piezoelectric response to finger press. **(b)** As-printed polarized spiral and corresponding piezoelectric response to vibration. Inset is a detailed voltage envelope inside the circled area.

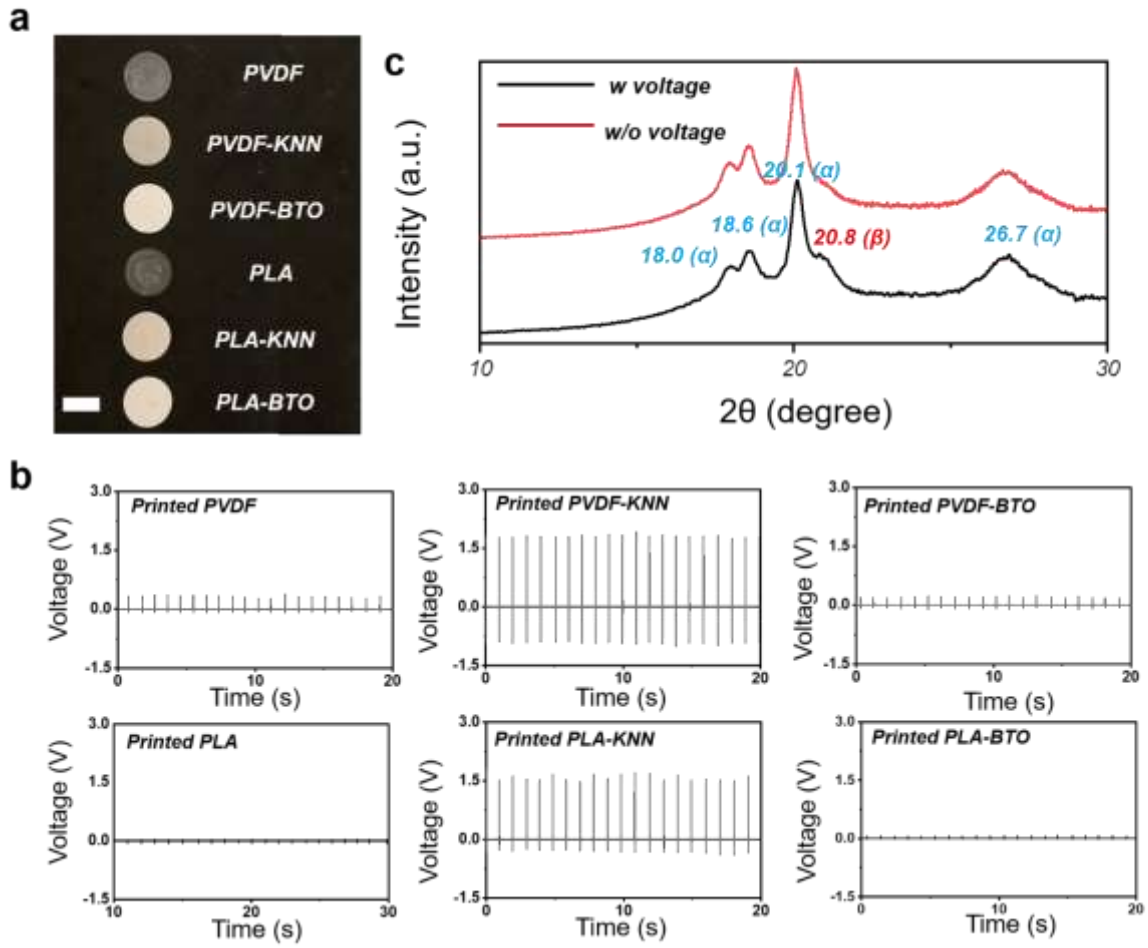


**Figure S7. (a)** Printed films with different compositions (From top to bottom: PVDF, PVDF-KNN, PVDF-BTO, PLA, PLA-KNN, PLA-BTO). The scale bar is 1 cm. **(b)** The voltage output of printed films under a mechanical force of 30 N at a frequency of 1 Hz. **(c)** XRD patterns of PVDF films printed with voltage and without voltage. In the range of 10°-30°, the unpoled printed PVDF has four characteristic peaks (18.0°, 18.6°, 20.1°, 26.7°) originating from α phase. An apparent new peak at 2θ = 20.8° appears in printed PVDF under voltage that is attributed to the poled electroactive β phase. This peak was also observed in the XRD pattern of printed PVDF-KNN composite

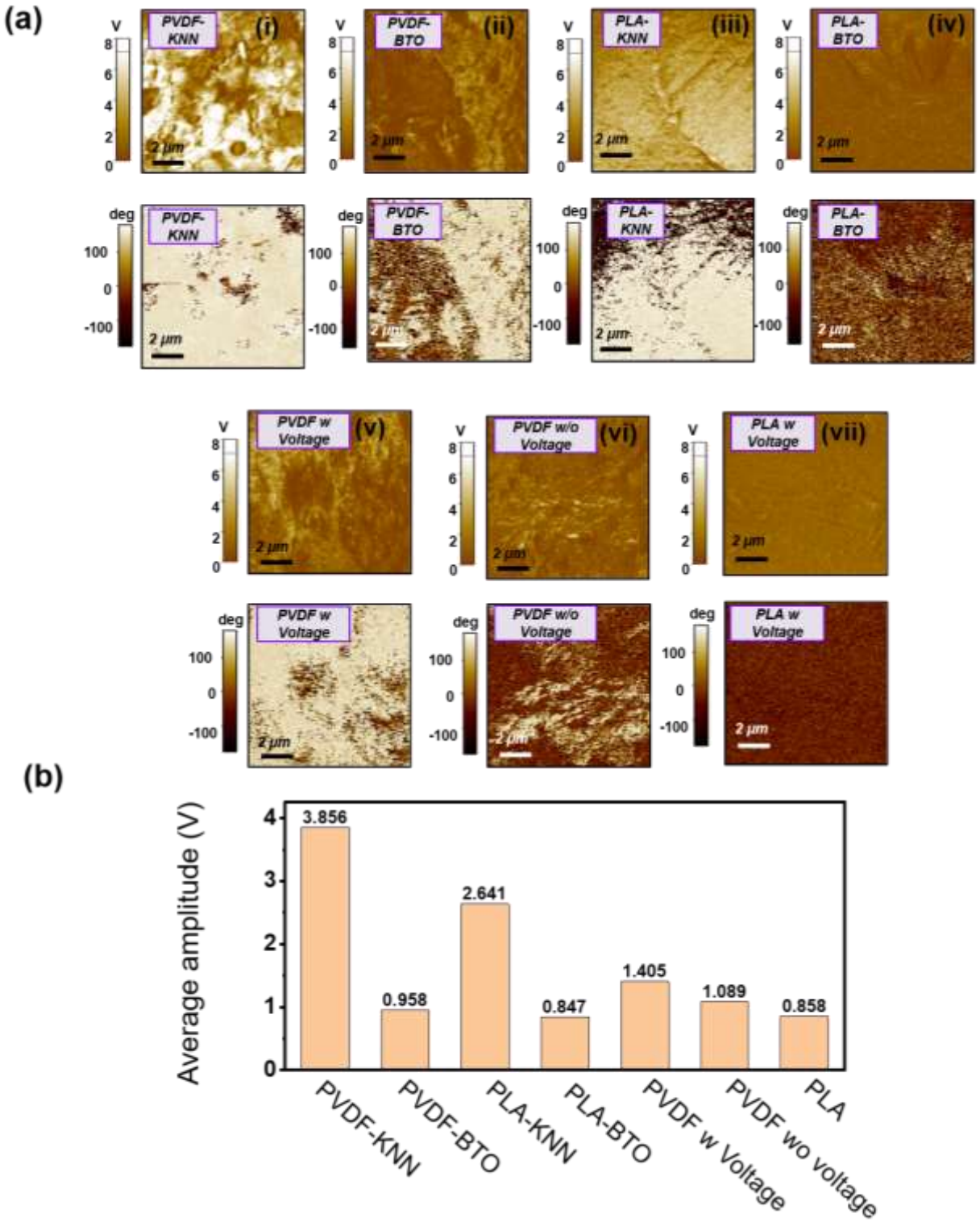


**Figure S8.** (a) EFM amplitude and phase image of printed films with different compositions **(i)** PVDF-KNN, **(ii)** PVDF-BTO, **(iii)** PLA-KNN, **(iv)** PLA-BTO, **(v)** PVDF printed with electric field, **(vi)** PVDF printed without electric field **(vii)** PLA with electric field. **(b)** Average amplitude values of all tested films. PVDF-KNN has the largest piezoelectric

response among four composite films. The stronger dipole in PVDF-KNN over PLA-KNN was due to the contribution from polarized PVDF, as revealed reasonable amplitude response in pure PVDF printed under electrical field compared to the pure PLA without detectable signals. Additionally, the EFM characterization validated that the amplitude signal in PVDF-BTO mostly arises from PVDF considering the rather weak signals in PLA-BTO film printed under the same condition. BTO was not effectively poled during high-temperature printing due to its low curie temperature (~120 ℃). In addition to amplitude image, phase image in Fig. 2f confirmed that PVDF-KNN has the narrowest phase distribution. While PLA-KNN and PVDF-BTO has significantly more positive phase than negative phase, the phase distribution in PLA-BTO was random, well corresponding to the amplitude image. The EFM amplitude variation of PVDF films printed with voltage (1.405 V) and without voltage (1.089 V) is not of significance. This phenomenon is in agreement with the fact that only a small portion of PVDF formed the β phase and was poled. It also matches with the result of small β phase peak in XRD in Figure 7c and the low voltage output of PVDF films in Figure 7b. It is the KNN that contributes major piezoelectric performance in the printed composite. All these evidences supported the presumption that synergistic effect based on the marriage of PVDF and KNN confers superior electromechanical coupling over other akin combinations.

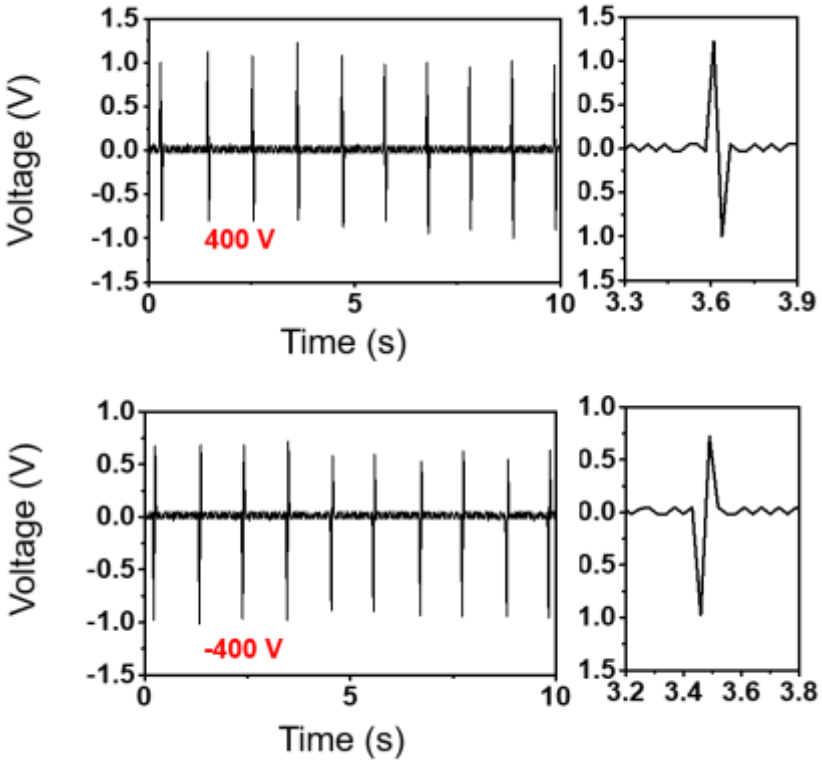


**Figure S9.** Voltage outputs of ferroelectric film printed under voltage of 400 V and -400 V, showing opposite polarity.

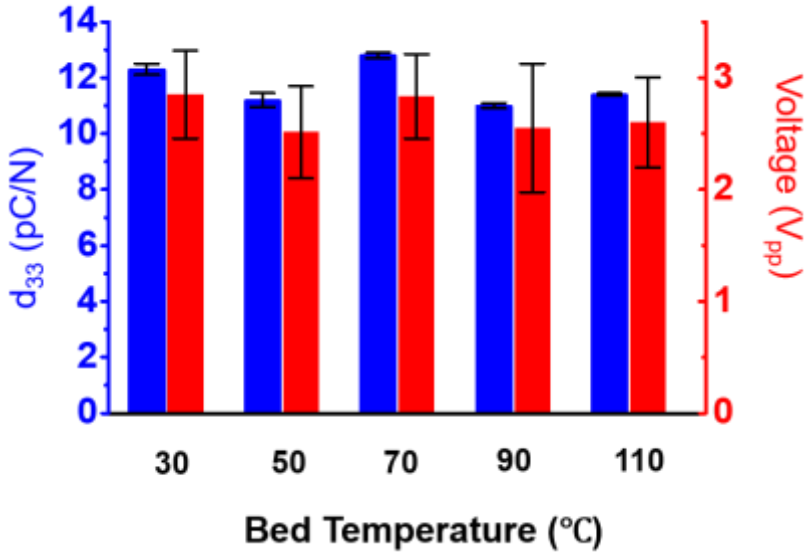


**Figure S10.** The piezoelectric coefficient d33 and peak-to-peak voltage output as a function of bed temperature. Data are expressed as mean ± SD (n = 3).

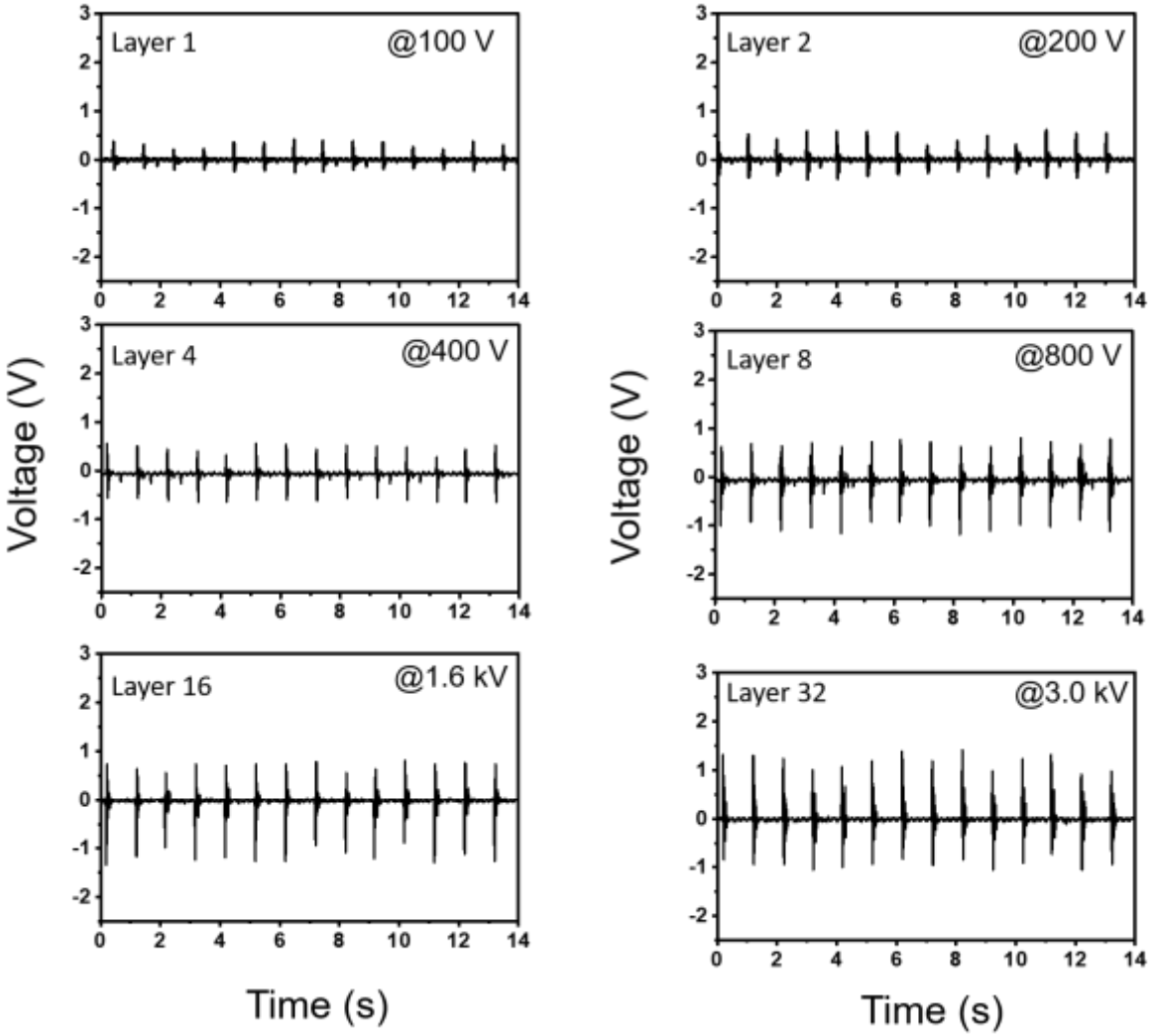


**Figure S11.** Comparison of voltage outputs of as-printed cylinders with different layers.

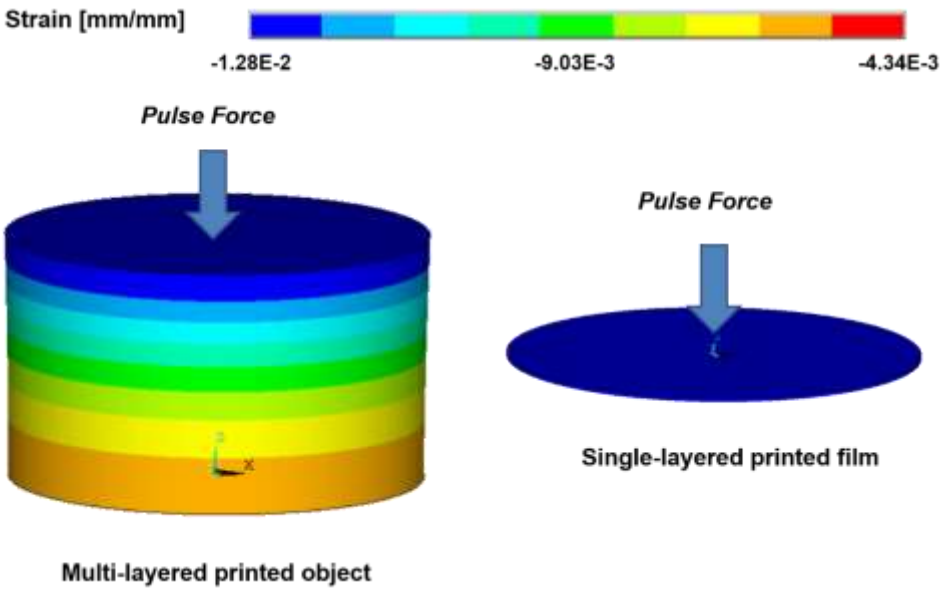


**Figure S12.** FEA simulations of strain distributions in printed multi-layered ferroelectric cylinder and single layer disc.

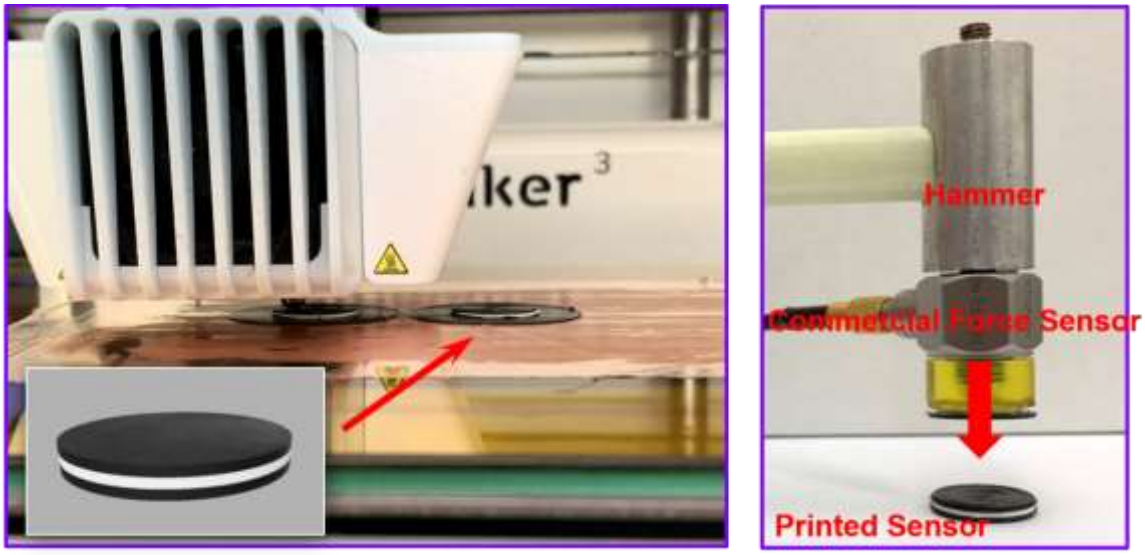


**Figure S13.** Direct print of ferroelectric device (left panel) and the pressure sensing test setup (right panel).

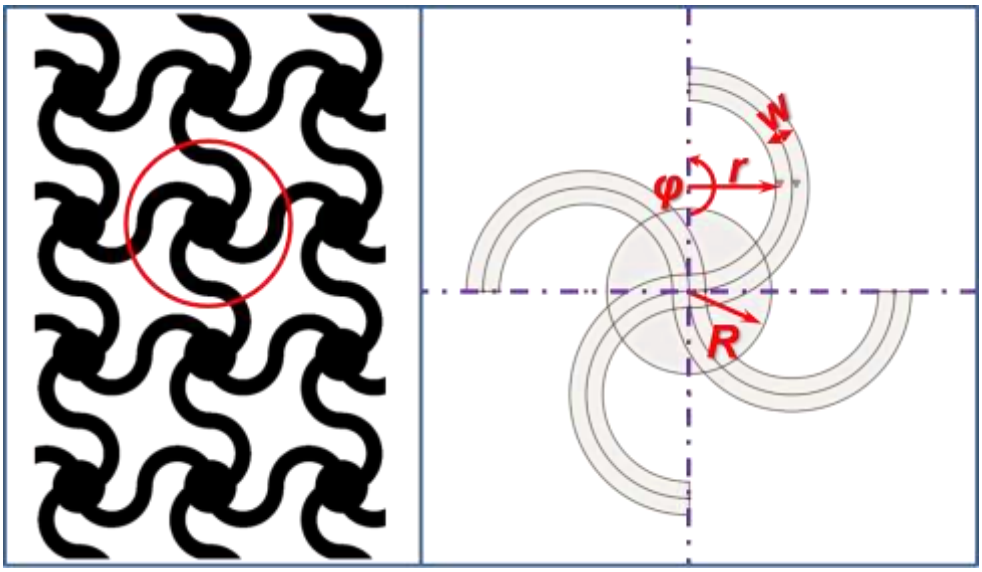


**Figure S14.** Detailed structure of sinusoidal lattice embedded in artificial artery. (R = 1.5 mm; r = 1.6 mm; W = 0.6 mm; ψ = 180 °C.)

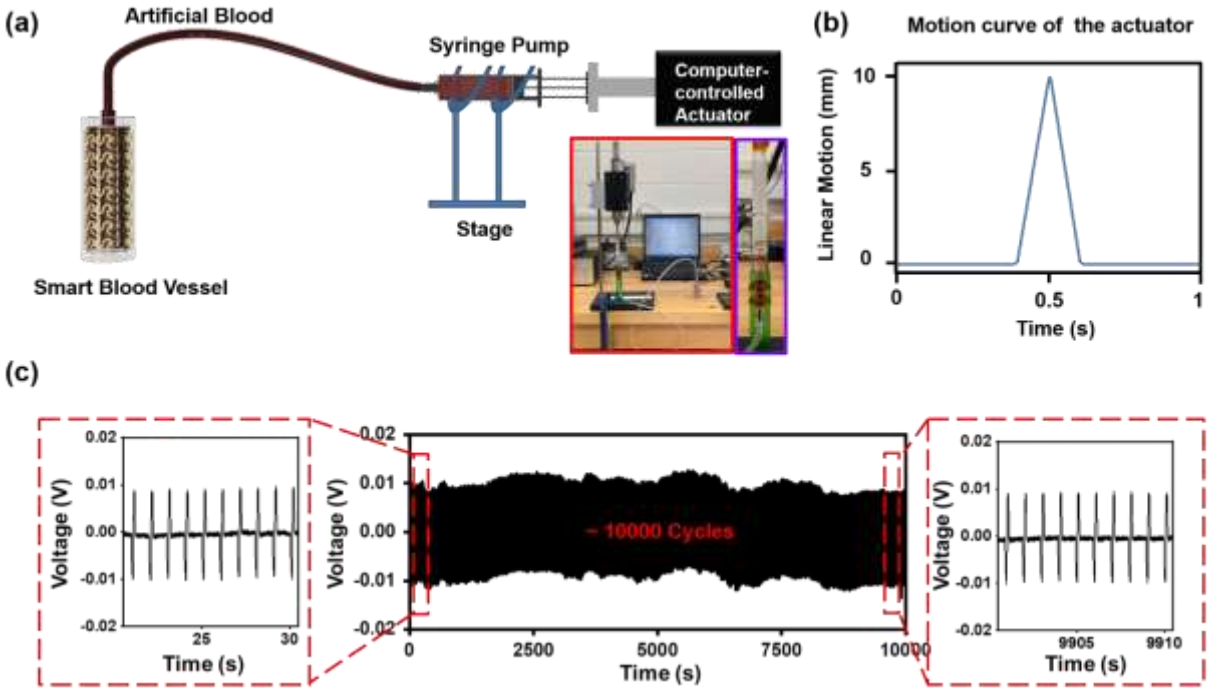


**Figure S15. (a)** The schematic illustration of smart blood vessel ith a syringe pump driven by a computer-controlled actuator. **(b)** The motion curve of the actuator in each cycle. **(c)** Long-term stability of artificial artery under artificial blood fluctuation with pressure change of 6 kPa (~45 mmHg) and at a frequency of 1 Hz. A stable output Vpp of ~ 19.55 mV was displayed with no significant reduction.

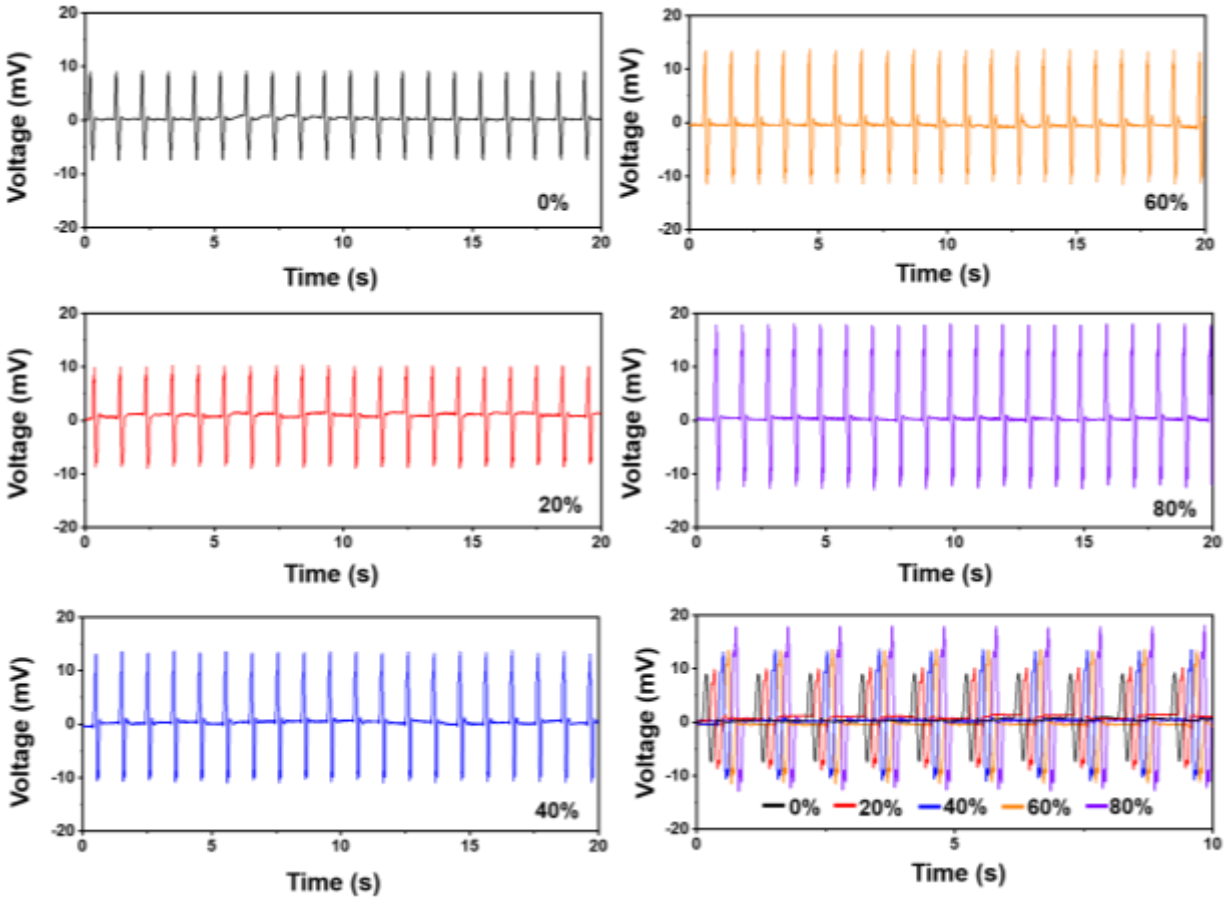


**Figure S16.** Voltage outputs of the ferroelectric artery at different levels of occlusion.

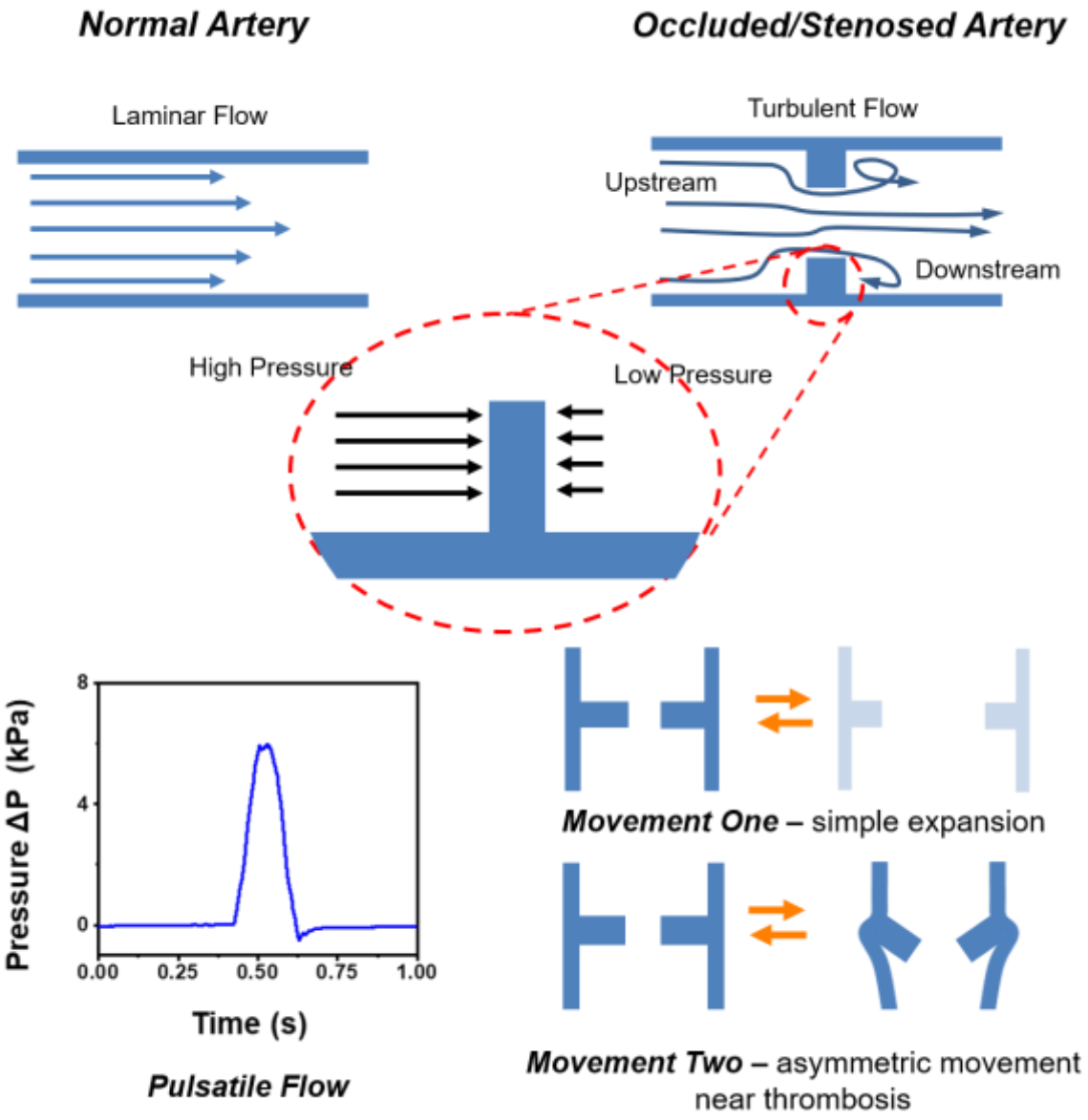


**Figure S17.** The mechanism of generation of two-peak voltage profile in partially occluded artery. Unlike that the normal artery has stable laminar flow, an unstable turbulent flow existed in occluded artery. This turbulent flow induces uneven and time-dependent pressure distribution between the two sides of thrombosis. While the normal artery has one movement of simple expansion and contraction under pulsatile pressure change, which generates one peak, the occluded artery will start generating the first peak once the upstream artery senses the pressure (movement one) and a second peak will be generated when the flow reaches the thrombosis and leads to the deformation of surrounding tissue (movement two). Extracting

and analyzing the features of this two-peak voltage profile may provide an avenue of detecting and diagnosing the location of thrombosis.

**Movies.**

**Movie S1.** FDM printing of ferroelectric composite under an electric field of 4 kV/mm.

**Movie S2.** Syringe pump-driven ferroelectric artery system mimicking heart beats.

**Movie S3.** Piezoelectric responses of the smart artery with electrodes connected forwardly.

**Movie S4.** Piezoelectric responses of the smart artery with electrodes connected reversely.

**Movie S5.** The motion of the artery filled with red-colored PBS-simulated blood under a $\Delta P$ of ~6 kPa.

**Movie S6.** Piezoelectric response of the artery filled simulated blood driven by a syringe pump.